Journal of Zhejiang University-SCIENCE A (Applied Physics & Engineering)
ISSN 1673-565X (Print); ISSN 1862-1775 (Online)
www.jzus.zju.edu.cn; www.springerlink.com
E-mail: jzus@zju.edu.cn

Influence of angle of attack on a combined opposing jet and platelet transpiration cooling blunt nose in hypersonic vehicle

Bin-xian SHEN[1,2], Hong-peng LIU[†‡2], Wei-qiang LIU[2]

[1]*China Computational Aerodynamics Institute, China Aerodynamics Research and Development Center, Mianyang 621000, China*

[2]*Science and Technology on Scramjet Laboratory, College of Aerospace Science and Engineering, National University of Defense Technology, Changsha 410073, China*

[†]E-mail: lhp81-1@163.com

Received Nov. 14, 2019; Revision accepted Apr. 18, 2020; Crosschecked July 15, 2020

Abstract: Flying condition with angle of attack is inevitable in a hypersonic vehicle, and it may influence the thermal protection system (TPS) performance of opposing jet and its combinations. A 3D Navier–Stokes equation and shear stress transfer (SST) k-ω model with compressible correction are employed to simulate the angle of attack characteristics of a blunt body with opposing jet and platelet transpiration TPS. The flowfield and heat flux transfer for angles of attack 0°, 3°, 6° with jet pressure ratio PR=0.1 and 0°, 6°, 12° with PR=0.2 are obtained. Numerical results show that the flowfield is no longer symmetrical with the effect of the angle of attack. The flowfield and heat transfer in windward and leeward performed adversely. The recompression shock wave in windward is strengthened, which increases local temperature and strengthens heat transfer. The opposing jet fails in thermal protection when the angle of attack reaches critical value; however, the critical angle of attack can be promoted by increasing PR. Finally, the transpiration gas can strengthen the cooling efficiency of windward, thereby, increasing the critical angle of attack.

Key words: Thermal protection; Opposing jet; Platelet transpiration; Angle of attack
https://doi.org/10.1631/jzus.A1900514 **CLC number:** V423

1 Introduction

The nose-tip of hypersonic vehicles can experience extreme aerodynamic heating when flying in high speed. Accumulated heating can destroy the structures and flying systems if not effectively dissipated. Therefore, hypersonic vehicles must have an effective and reliable thermal protection system (TPS) to be able to efficiently reach cruise speed.

TPS methods for hypersonic vehicles fall into three categories: passive, semi-passive, and active. The material structure and ablation TPS currently applied in real flights belong to the passive and semi-passive methods, respectively (Xie et al., 2013; Riccio et al., 2017). Although the ceramic matrix composites (Ferraiuolo et al., 2019) and hybrid carbon/carbon (C/C) composites (Zhang and Li, 2018) are now used as TPS in some vehicles, these traditional passive and semi-passive methods cannot accommodate the high-speed, long-term, and repetitive requirements of hypersonic vehicles. Only active methods, which can protect structures by controlling flowfield and introducing coolants, will be able to withstand long-term and high aerodynamic heating. Therefore, developing stable and effective active TPS methods is essential ingredient in designing future hypersonic vehicles.

Opposing jet is used as an active flowfield control technology in drag and heat flux reduction in hypersonic vehicles (Huang, 2015). The coolant enters from the injector facing the freestream and pushes the shock wave away from the wall surface. The

‡ Corresponding author
ORCID: Hong-peng LIU, https://orcid.org/0000-0002-1664-7517

opposing jet coolant then stops because of the freestream and forms a recirculation region around the jet, as a recompressed shock forms next to the recirculation region boundary. Extreme aerodynamic heating often occurs behind the shock wave and is strongly related to shock wave intensity. In an opposing jet flow, aerodynamic heating is insulated by low-temperature recirculation flow that significantly reduces the wall heat flux (Warren, 1960). Thermal protection performance of opposing jet methods has been used in wind tunnel testing (Wang et al., 2016). Hayashi et al. (2006) proved that using opposing jets methods can reduce maximum heat flux by more than 50% than that without injection. Imoto et al. (2011) showed that opposing jet methods can reduce the heat flux stagnation point by over 80% while other researchers have reviewed numerical simulations that show the excellent heat flux reduction of opposing jet methods (Sun et al., 2019). Other research has shown that cooling efficiency can be influenced by operating conditions and physical dimensions, such as jet properties (Huang et al., 2018; Shen et al., 2018) and injector configurations (Barzegar Gerdroodbary et al., 2015; Li et al., 2017). Other thermal protection techniques such as spike (Zhu et al., 2018) and forward-facing cavity (Lu and Liu, 2013) have also been considered as approaches to improve the efficiency of thermal protection in opposing jet TPS. These combined TPS methods could promote thermal protection capacity and reduce coolant flux.

When vehicles fly with an angle of attack, an angle occurs between the opposing jet and freestream flows. The stagnation point of freestream deviates from the opposing jet. Consequently, the thermal protection performance between windward and leeward sides can have different properties. Zhou and Ji (2014) investigated the flow structure of unsteady oscillatory motion mode with an angle of attack in an opposing jet flow, showing that the shock stand-off distance is significantly shortened with increased angle of attack, and the reattachment shock wave on the windward side moves upstream. Daso et al. (2009) tested the 2.6%-scale Apollo capsule model in a wind tunnel of supersonic freestream showing that thermal protection decreases with increased angle of attack, but the opposing jet still cools vehicles even at a 9° angle of attack. Lu and Liu (2012) analyzed the influence of angle of attack on opposing jet TPS numerically finding that angle of attack weakens the cooling efficiency of the opposing jet on the windward side, and that the maximum heat flux exceeds the heat flux at stagnation without injection when the angle of attack is sufficiently large. The opposing jet TPS then becomes invalid. The cooling efficiency in windward can be enhanced by strengthening injection intensity, which simultaneously increases the mass flux of coolant. The thermal protection structures in windward could be improved to increase local cooling efficiency where the maximum heat flux occurs to entirely avoid increasing the intensity of the opposing jet.

A platelet transpiration device is considered to overcome the problem (Shen et al., 2019). The transpiration coolant gas is introduced on the windward side to strengthen local cooling efficiency while the opposing jet protects the entire nose-tip from aerodynamic heating especially in the stagnation region.

In this paper, we present a numerical study of a combined opposing jet and platelet transpiration blunt body conducted to (1) explore the influences of angle of attack on flowfield in combined TPS, (2) better understand the influence of angle of attack on heat transfer in combined TPS, and (3) document the thermal protection performance of the combined TPS with the effect of angle of attack.

2 Physical model

2.1 Geometrical model

The combined opposing jet and platelet transpiration TPS are shown in Fig. 1 and its sizes are shown in Table 1. Combinational structures are mainly organized by platelet devices and combine two parts, including opposing jet and platelet transpiration systems. The radius of the blunt body R_n is 25 mm. The injector of the opposing jet is located at the stagnation point of the blunt body, with a radius R_j of 2 mm. The transpiration orifices are bored on the reattachment region of opposing jet and the pipeline is arranged in the interior while the passages for transpiration coolants are installed around the opposing jet pipeline. The transpiration orifices are hierarchically arrayed and each platelet contains six coolant injection orifices. Ten platelets are available, and the injectors of the adjacent platelet are staggered. L_s and W_s

represent for the thickness of the platelet and the width of the orifices, respectively. W_s is defined as

$$W_s = C_1\sqrt{R_n^2 - (R_n - L_o - 0.25L_s)^2}, \quad (1)$$

where C_1 is a design parameter related to structures of blunt body and transpiration orifices. L_o represents the distance between the platelet and stagnation point.

In the actual manufacturing process, the size of transpiration orifices should be smaller, and the number of the orifices should be increased. Thus, the interlaced orifices can cool more surface to ensure good cooling performance. In this paper, structures are simplified with limited numbers and big sizes of orifices to avoid enormous calculation workload.

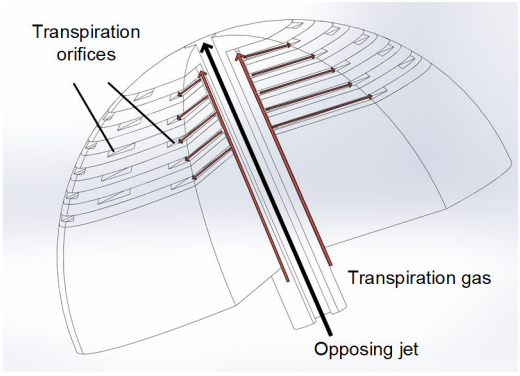

Fig. 1 Structures of combinational opposing jet and platelet transpiration blunt body

Table 1 Parameters of the combined blunt body

Parameter	Value
R_n (mm)	25
R_j (mm)	2
C_1	0.26
L_s (mm)	0.35
L_o (mm)	2.7

2.2 Flow parameters

The boundary conditions are shown in Table 2. There are three types of inlet boundaries for combined blunt body. The incoming freestream is assumed as the far-field boundary condition, and the freestream is at a height of 25 km and a Mach number of 6 with the static pressure and temperature of 2549 Pa and 221 K, respectively. Then, the opposing jet is described by a pressure inlet, its total pressure is set according to the jet pressure ratio (PR), and its static pressure is calculated to ensure the Mach number of the opposing jet (Ma_j=1). The PR is defined by the total pressures of the opposing jet and freestream:

$$\mathrm{PR} = \frac{p_{0,j}}{p_{0,\infty}}, \quad (2)$$

where $p_{0,j}$ and $p_{0,\infty}$ represent the total pressures of the opposing jet and freestream, respectively. The last boundary is mass-flow boundary for the transpiration coolant gas. The mass flux of the coolants is determined by a controllable mass flux ratio between the opposing jet and transpiration coolants (m_{jet}/m_{tran}). Finally, the isothermal wall is assumed to be at a temperature of 295 K.

Table 2 Flow parameters

Parameter	Value
Freestream Mach number, Ma_∞	6
Freestream static pressure, P_∞ (Pa)	2549
Freestream static temperature, T_∞ (K)	221
Opposing jet Mach number, Ma_j	1
Jet pressure ratio, PR	0.1, 0.2
Mass flux of transpiration gas, m_{tran}	$0.1m_{jet}$
Coolant total temperature, $T_{0,c}$ (K)	300
Wall temperature, T_w (K)	295

3 Numerical approach

The 3D Reynolds-averaged Navier–Stokes equations are considered as the governing equations to calculate the flow characteristics of the combined blunt body while the shear stress transfer (SST) k-ω model with compressible correction is used to describe turbulence characteristics. The SST k-ω model, combining both the stability of original k-ω near the wall surface and the independence of standard k-ε models in outer space, is insensitive to the specification of freestream turbulence level (Edalatpour et al., 2019). The governing equations are solved with a density-based coupled double-precision solver in the ANSYS Fluent 16.0. The inviscid fluxes are computed by the advection upstream splitting method (AUSM) flux vector splitting with a first spatially accurate upwind scheme while the viscous fluxes are computed by the first-order upwind scheme (Barzegar

Gerdroodbary et al., 2017). The full implicit lower-upper symmetric Gauss-Seidel (LU-SGS) method is used for time integration with a local time step.

4 Validation of numerical models

4.1 Grid analysis

Appropriate grid organization is necessary to calculate sound results, especially in simulating surface heat transfer. The calculated space is filled with hexahedron elements. The height of first layer is 0.000 005 m with a stretching factor of 1.05 to ensure the $y+$ is less than 1 near the surface. Thus, three types of grid, namely coarse mesh, moderate mesh, and refined mesh are evaluated in this section. Their mesh number is 4 976 640 (120×192×216, 120 points along the axis direction, 192 points along the body surface, and 216 points along the tangential direction), 6 273 280 (130×208×232), and 7 673 120 (140×221×248), respectively. Sketch diagrams of the grid system are shown in Fig. 2. Pivotal structures such as opposing orifices and locations where the bow shock wave occurs are arranged with detailed cells. Fig. 3 shows the distributions of wall heat flux with different meshes, illustrating that obvious differences are difficult to distinguish as the grid varies from coarse mesh to refined mesh. The figure shows that the three kinds of grids yield similar results in terms of calculating heat transfer. We therefore use a moderate grid to perform the solving procedure to promote calculation efficiency.

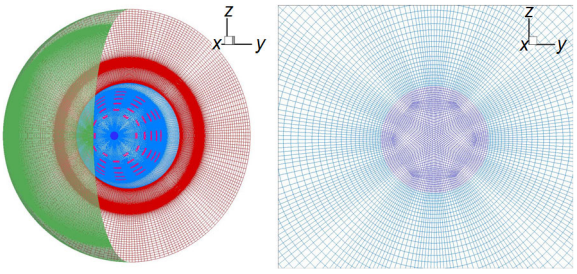

Fig. 2 Grid information

4.2 Validation of numerical models

The numerical methods are validated by referencing the opposing jet model of Hayashi et al. (2005)'s test. The freestream and opposing jet conditions in Hayashi et al. (2005)'s test are listed in Table 3, and the case of PR=0.4 is used to ensure a typical stable flowfield. Fig. 4 shows the density comparison of the predicted results and the experimental data. Representative structures of the opposing jet such as bow shockwave, recompression shockwave, Mach disk, and recirculation flow are recognized clearly in the calculated density contour. Additionally, these structures exhibit good similarity to the experimental Schlieren. Only slight discrepancies are observed on bow shockwave and Mach disk. The stand-off distance in the simulation is minimal compared to the experimental data.

Fig. 5 compares the Stanton number (St) distributions along the surface between the predicted results by computational fluid dynamics (CFD) and experimental data, where St is defined as

$$St=\frac{q_{\mathrm{w}}}{(T_{\mathrm{aw}}-T_{\mathrm{w}})\rho_{\infty}c_{\mathrm{p}\infty}u_{\infty}}, \tag{3}$$

$$T_{\mathrm{aw}}=T_{\infty}\left[1+\sqrt[3]{Pr_{\mathrm{w}}}\left(\frac{\gamma-1}{2}Ma_{\infty}^{2}\right)\right], \tag{4}$$

where q_{w} stands for the wall heat flux; T_{aw} stands for the adiabatic wall temperature; ρ_{∞} and u_{∞} denote the density and velocity of freestream, respectively; $c_{\mathrm{p}\infty}$ stands for the specific heat of freestream; Pr_{w} and γ indicate the Prandtl number and the ratio of specific heats. Besides, a parameter E_{q} is calculated to estimate the numerical error quantitatively.

$$E_{\mathrm{q}}=\frac{St_{\mathrm{CFD}}-St_{\mathrm{exp}}}{St_{\mathrm{exp,max}}}\times 100\%. \tag{5}$$

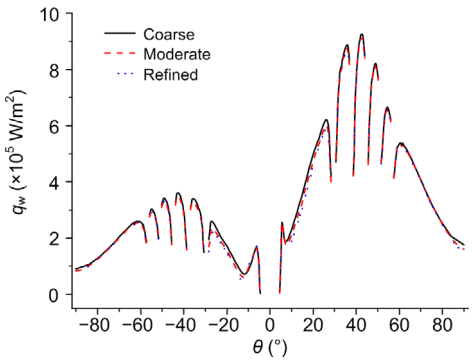

Fig. 3 Comparison of wall heat flux for different grids
θ is the spherical center angle for blunt surface relative to freestream direction (θ>0: windward; θ<0: leeward)

Table 3 Freestream and jet conditions of experiment

Freestream	Opposing jet	Wall
Ma_∞=3.98	Ma_j=1	
$p_{0,\infty}$=1.37 MPa	PR=0.4	T_w=295 K
$T_{0,\infty}$=397 K	$T_{0,j}$=300 K	

$T_{0,\infty}$ and $T_{0,j}$ denote the total temperatures of freestream and opposing jet, respectively

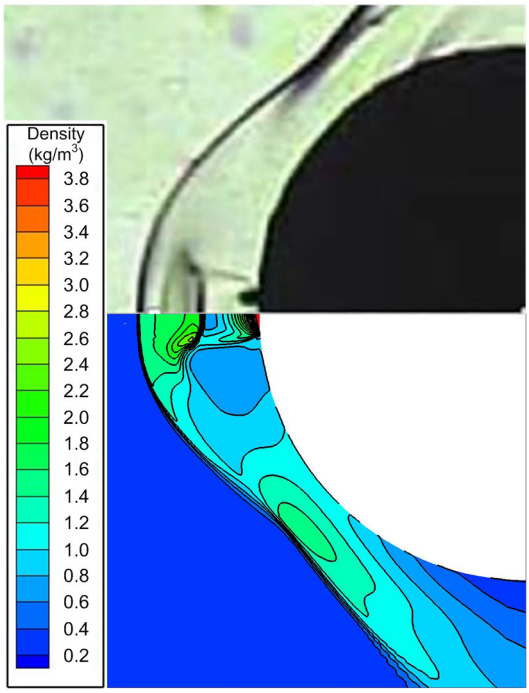

Fig. 4 Comparison of flowfields obtained by experimental data and predicted results

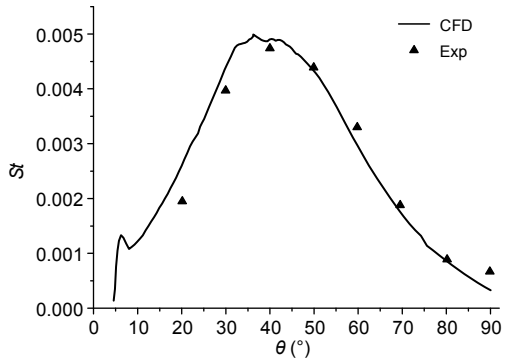

Fig. 5 Comparison of *St* between predicted results (CFD) and experimental data (exp)

St_{CFD} and St_{exp} are the Stanton numbers calculated by the numerical simulation and obtained from Hayashi et al. (2005)'s test, respectively. The predicted surface *St* distribution exhibits a similar tendency to the test data. The E_q in each point is then calculated with the maximum E_q of 14.3% occurring in the first test point. The errors in the pivotal reattachment regions, such as points 2–4, are below 10%. The discrepancies of 10% for heat flux are acceptable. Consequently, the numerical methods listed above are also acceptable to predict heat transfer in the opposing flow.

5 Results

5.1 Flowfield

Fig. 6 illustrates the Mach number distributions of the combined TPS with different angles of attack when PR=0.1 and 0.2. The stagnation point of the incoming freestream deviates from the central point of the blunt body under the influence of the angle of attack. As a result, the flowfield around the body is no longer symmetrical, forming differently on the windward and leeward sides. On the windward side, the recompressed shock wave becomes stronger influenced by the increased compression flow created by the increased angle of attack. By contrast, on the leeward side, the recompressed shock wave weakens gradually with the increase of angle of attack. The

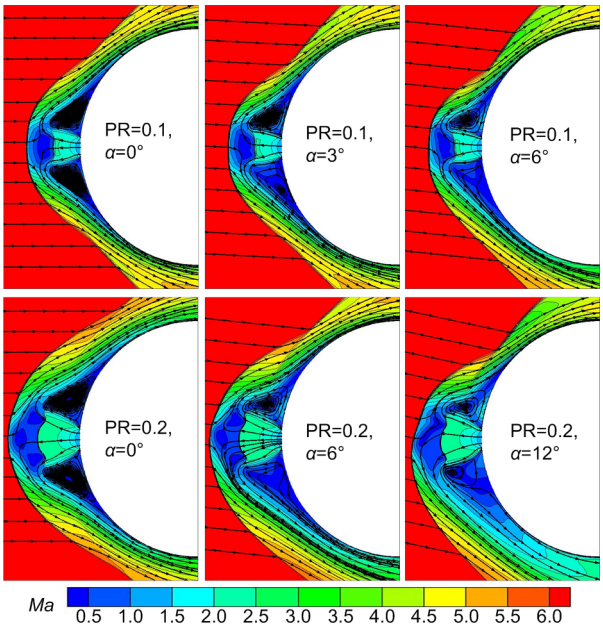

Fig. 6 Mach number distributions of combined TPS with different angles of attack (α)

bow shock wave is also influenced by the angle of attack, leaning towards the windward side and pushing the recirculation region upward. Simultaneously, the recirculation region on the leeward side expands and is dragged to the backside. Fig. 7 shows the temperature distributions of the combined TPS with different angles of attack when PR=0.1 and 0.2. Temperature discrepancies with different angles of attack occur behind the recompression shock wave on the windward side. Temperature increases with the influence of the stronger recompression shock wave when the angle of attack increases. The locations of the recompression shock wave and the reattachment point gradually deviate when the angle of attack is increased to 6° with PR=0.1 and 12° with PR=0.2. As a result, two local high-temperature regions occur in the reattachment point and behind the recompression shock wave, respectively.

The intensity of the opposing jet also affects the flowfield characteristics of the combined blunt body with the angle of attack. The influence of the angle of attack on the flowfield weakens with increased angle of attack. In Fig. 7, the temperature distribution of PR=0.2, α=6° is consistent with that of PR=0.1, α=3°, and the temperature distribution of PR=0.2, α=12° is consistent with that of PR=0.1, α=6°. The insulating capacity of the opposing jet could be strengthened with a stronger opposing jet. For this reason, the opposing jet TPS could endure the increased forceful compression of recompression shock wave.

Fig. 8 shows the temperature comparisons between the opposing jet TPS and combined TPS. Macroscopic analysis shows that these two kinds of TPS have similar flowfield structures. The locations of the bow and recompression shock waves, as well as the maximum temperature of the flow, are consistent. The transpiration coolant injected along the redial direction of the platelet is too weak to penetrate the far flowfield and therefore cannot change the macroscopic flowfield. The affected region of transpiration is limited in the local region around the orifices. A thin smooth boundary adhering to the body surface on the force of reattachment flow in opposing jet flow is available, but is broken up by the injected transpiration gas in combined TPS. The transpiration gas hits against the reattachment flow and forms an embossment that covers the orifices. The injected low-temperature transpiration gas improves the thermal environment around the orifices. Furthermore, the low-temperature transpiration gas also reduces the local temperature behind the recompression shock wave in combined TPS, making the temperature with transpiration lower than that without transpiration.

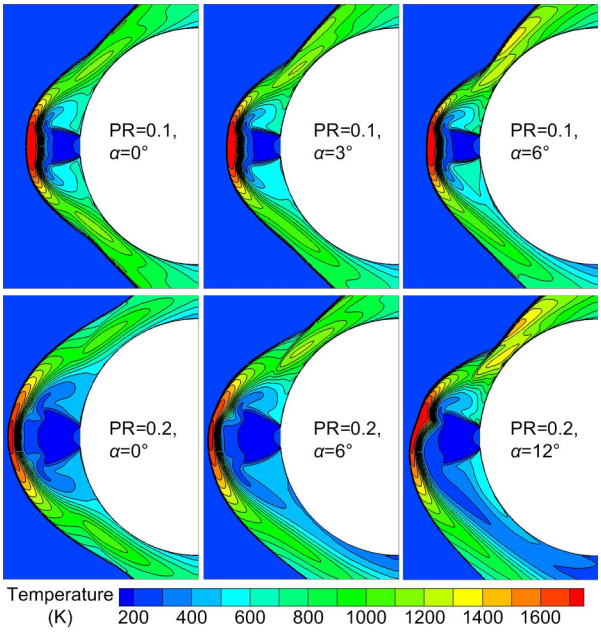

Fig. 7 Temperature distributions of combined TPS with different angles of attack

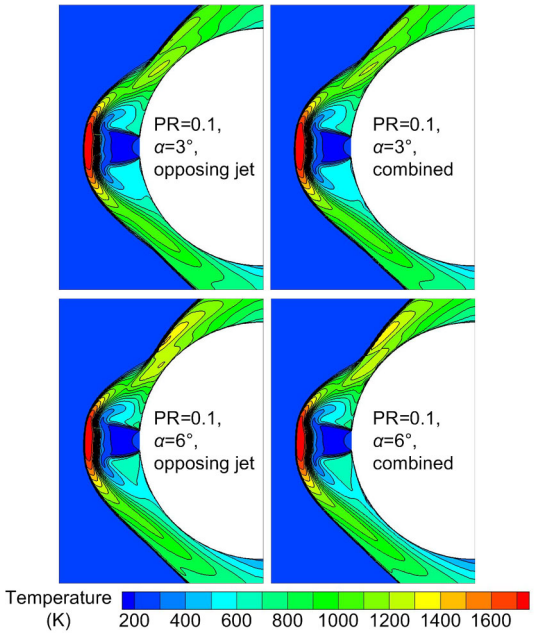

Fig. 8 Temperature distribution comparisons between the opposing jet TPS and combined TPS

5.2 Heat transfer

Figs. 9 and 10 show the temperature comparisons of recompression shock wave in the windward between the opposing jet TPS and combined TPS with different angles of attack when PR=0.1 and 0.2, respectively. The temperature and temperature gradient in near-wall regions are affected by the angle of attack and transpiration gas. Firstly, the temperature and temperature gradient increase with stronger compression of the recompression shock wave with increased angle of attack on the windward side. The temperature in near-wall regions decreases with the insulating and absorbing heat of transpiration coolant, improving the thermal properties near the wall.

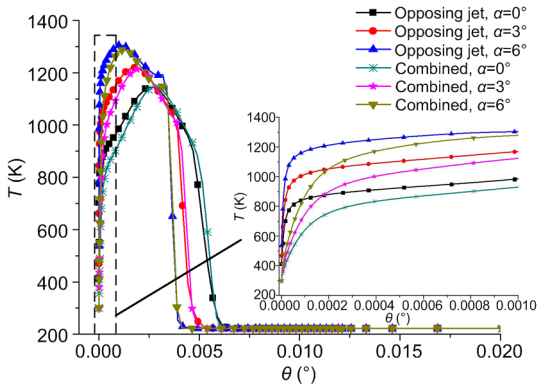

Fig. 9 Temperature comparisons between the opposing jet TPS and combined TPS with different angles of attack when PR=0.1

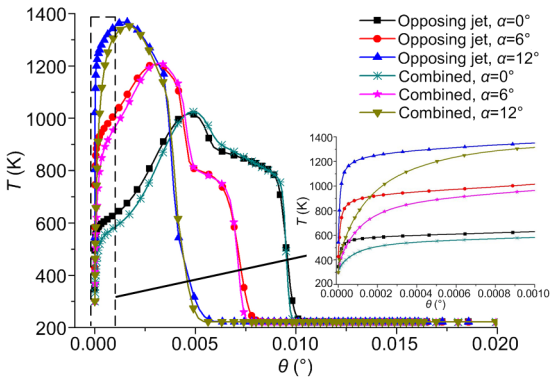

Fig. 10 Temperature comparisons between the opposing jet TPS and combined TPS with different angles of attack when PR=0.2

Figs. 11 and 12 show the heat flux in the windward and leeward generatrix with different angles of attack when PR=0.1 and 0.2, respectively. The heat flux is compared with and without injection when the angle of attack is 0°. The heat flux in the windward increases remarkably with the influence of angle of attack, and thus, thermal protection intensity should be strengthened in the windward. By contrast, thermal protection intensity could be weakened in the leeward. The maximum heat flux is closer to the stagnation heat flux than TPS without opposing jet when the angle of attack reaches 6° with PR=0.1. This finding means that the opposing jet TPS has lost its efficacy. The figure shows that the opposing jet TPS cannot cool the blunt body when the angle of attack is 6° with PR=0.1, while it still cools the blunt body when the angle of attack is 6° with PR=0.2, which indicates that the cooling efficiency could be enhanced by promoting PR.

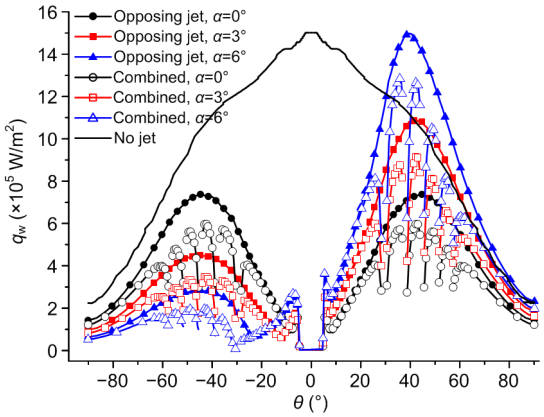

Fig. 11 Influence of angle of attack on heat flux in windward and leeward when PR=0.1

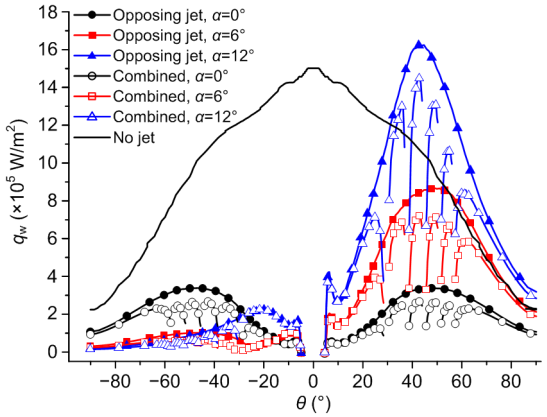

Fig. 12 Influence of angle of attack on heat flux in windward and leeward when PR=0.2

The heat flux with combined TPS is reduced in the windward than that without transpiration in Figs. 11 and 12. For example, the combined TPS persistently cools the blunt body when PR=0.1, α=6°, while the opposing jet TPS has lost its efficacy with the same PR and angle of attack. Table 4 shows the comparisons of maximum heat flux between the opposing jet TPS and combined TPS. The maximum heat flux reduces more than 10% with combined TPS, and the maximum reduction of combined TPS reaches 21.07% when PR=0.2, α=0°.

Table 4 Comparisons of maximum heat flux between opposing jet TPS and combined TPS

PR	α (°)	$q_{j,max}$ (W/m^2)	$q_{c,max}$ (W/m^2)	$\frac{q_{j,max}-q_{c,max}}{q_{j,max}}$
0.1	0	737 178	598 974	18.74%
0.1	3	1 088 860	917 436	15.74%
0.1	6	1 497 830	1 284 560	14.24%
0.2	0	338 576	267 222	21.07%
0.2	6	867 680	721 151	16.88%
0.2	12	1 623 990	1 449 300	10.75%

$q_{j,max}$ denotes the maximum heat flux of opposing jet TPS; $q_{c,max}$ denotes the maximum heat flux of combined TPS

6 Conclusions

This numerical study of heat flux reduction in hypersonic flow shows the influence of angle of attack on opposing jet TPS and combined TPS including data on flowfields and heat transfer. The study shows:

1. The flowfield is no longer symmetrical with the effect of angle of attack. The recompression shock wave is strengthened on the windward side with increased angle of attack along with the temperature behind the recompression shock wave, and is inverse on the leeward.

2. The heat flux increases in the windward with the increased angle of attack, exacerbating the thermal environment of vehicles. The TPS loses its efficiency when the angle of attack is large enough, and then the maximum heat flux is bigger than that without TPS. Besides, the critical angle of attack at which the TPS loses its efficiency could be enhanced by increasing the intensity of the opposing jet (PR).

3. The transpiration gas could improve the thermal protection properties of the windward side in combined TPS, and the maximum heat flux reduction could reach 21.07% of that without transpiration.

Contributors

Hong-peng LIU designed the research. Bin-xian SHEN processed the corresponding data and wrote the first draft of the manuscript. Wei-qiang LIU helped to organize the manuscript. Bin-xian SHEN revised and edited the final version.

Conflict of interest

Bin-xian SHEN, Hong-peng LIU, and Wei-qiang LIU declare that they have no conflict of interest.

References

Barzegar Gerdroodbary M, Imani M, Ganji DD, 2015. Investigation of film cooling on nose cone by a forward facing array of micro-jets in hypersonic flow. *International Communications in Heat and Mass Transfer*, 64:42-49. https://doi.org/10.1016/j.icheatmasstransfer.2015.02.015

Barzegar Gerdroodbary M, Amini Y, Ganji DD, et al., 2017. The flow feature of transverse hydrogen jet in presence of micro air jets in supersonic flow. *Advances in Space Research*, 59(5):1330-1340. https://doi.org/10.1016/j.asr.2016.11.040

Daso EO, Pritchett VE, Wang TS, et al., 2009. Dynamics of shock dispersion and interactions in supersonic freestreams with counterflowing jets. *AIAA Journal*, 47(6):1313-1326. https://doi.org/10.2514/1.30084

Edalatpour A, Hassanvand A, Barzegar Gerdroodbary M, et al., 2019. Injection of multi hydrogen jets within cavity flameholder at supersonic flow. *International Journal of Hydrogen Energy*, 44(26):13923-13931. https://doi.org/10.1016/j.ijhydene.2019.03.117

Ferraiuolo M, Scigliano R, Riccio A, et al., 2019. Thermo-structural design of a ceramic matrix composite wing leading edge for a re-entry vehicle. *Composite Structures*, 207:264-272. https://doi.org/10.1016/j.compstruct.2018.09.024

Hayashi K, Aso S, Tani Y, 2005. Numerical study of thermal protection system by opposing jet. Proceedings of the 43rd AIAA Aerospace Sciences Meeting and Exhibit. https://doi.org/10.2514/6.2005-188

Hayashi K, Aso S, Tani Y, 2006. Experimental study on thermal protection system by opposing jet in supersonic flow. *Journal of Spacecraft and Rockets*, 43(1):233-235. https://doi.org/10.2514/1.15332

Huang W, 2015. A survey of drag and heat reduction in supersonic flows by a counterflowing jet and its combinations. *Journal of Zhejiang University-SCIENCE A (Applied Physics & Engineering)*, 16(7):551-561. https://doi.org/10.1631/jzus.A1500021

Huang W, Zhang RR, Yan L, et al., 2018. Numerical experiment on the flow field properties of a blunted body with a counterflowing jet in supersonic flows. *Acta Astronautica*,

147:231-240.
https://doi.org/10.1016/j.actaastro.2018.04.018

Imoto T, Okabe H, Tani Y, 2011. Enhancement of aerodynamic heating reduction in high enthalpy flows with opposing jet. Proceedings of the 49th AIAA Aerospace Sciences Meeting Including the New Horizons Forum and Aerospace Exposition.
https://doi.org/10.2514/6.2011-346

Li SB, Wang ZG, Huang W, et al., 2017. Analysis of flowfield characteristics for equal polygon opposing jet on different freeflow conditions. *Acta Astronautica*, 133:50-62.
https://doi.org/10.1016/j.actaastro.2017.01.011

Lu HB, Liu WQ, 2012. Numerical investigation on properties of attack angle for an opposing jet thermal protection system. *Chinese Physics B*, 21(8):084401.
https://doi.org/10.1088/1674-1056/21/8/084401

Lu HB, Liu WQ, 2013. Investigation of thermal protection system by forward-facing cavity and opposing jet combinatorial configuration. *Chinese Journal of Aeronautics*, 26(2):287-293.
https://doi.org/10.1016/j.cja.2013.02.005

Riccio A, Raimondo F, Sellitto A, et al., 2017. Optimum design of ablative thermal protection systems for atmospheric entry vehicles. *Applied Thermal Engineering*, 119:541-552.
https://doi.org/10.1016/j.applthermaleng.2017.03.053

Shen BX, Liu WQ, Yin L, 2018. Drag and heat reduction efficiency research on opposing jet in supersonic flows. *Aerospace Science and Technology*, 77:696-703.
https://doi.org/10.1016/j.ast.2018.03.051

Shen BX, Yin L, Zhang XL, et al., 2019. Investigation on cooling effect with a combinational opposing jet and platelet transpiration concept in hypersonic flow. *Aerospace Science and Technology*, 85:399-408.
https://doi.org/10.1016/j.ast.2018.11.021

Sun XW, Huang W, Ou M, et al., 2019. A survey on numerical simulations of drag and heat reduction mechanism in supersonic/hypersonic flows. *Chinese Journal of Aeronautics*, 32(4):771-784.
https://doi.org/10.1016/j.cja.2018.12.024

Wang ZG, Sun XW, Huang W, et al., 2016. Experimental investigation on drag and heat flux reduction in supersonic/hypersonic flows: a survey. *Acta Astronautica*, 129:95-110.
https://doi.org/10.1016/j.actaastro.2016.09.004

Warren CHE, 1960. An experimental investigation of the effect of ejecting a coolant gas at the nose of a bluff body. *Journal of Fluid Mechanics*, 8(3):400-417.
https://doi.org/10.1017/S0022112060000694

Xie GN, Wang Q, Sunden B, et al., 2013. Thermomechanical optimization of lightweight thermal protection system under aerodynamic heating. *Applied Thermal Engineering*, 59(1-2):425-434.
https://doi.org/10.1016/j.applthermaleng.2013.06.002

Zhang B, Li XD, 2018. Numerical simulation of thermal response and ablation behavior of a hybrid carbon/carbon composite. *Applied Composite Materials*, 25(3):675-688.
https://doi.org/10.1007/s10443-017-9645-1

Zhou CY, Ji WY, 2014. A three-dimensional numerical investigation on drag reduction of a supersonic spherical body with an opposing jet. *Proceedings of the Institution of Mechanical Engineers, Part G: Journal of Aerospace Engineering*, 228(2):163-177.
https://doi.org/10.1177/0954410012468539

Zhu L, Chen X, Li YG, et al., 2018. Investigation of drag and heat reduction induced by a novel combinational lateral jet and spike concept in supersonic flows based on conjugate heat transfer approach. *Acta Astronautica*, 142:300-313.
https://doi.org/10.1016/j.actaastro.2017.11.001

中文概要

题　目： 高超声速飞行器逆向射流与层板发汗组合热防护的攻角特性分析

目　的： 采用层板发汗技术改善高超声速飞行器在攻角飞行时迎风面逆向射流的热防护性能。

创新点： 1. 提出逆向射流与层板发汗组合热防护方案用于高超声速飞行器的热防护；2. 采用层板发汗技术改进高超声速飞行器在大攻角飞行时热防护失效的不足。

方　法： 1. 设计逆向射流与层板发汗组合热防护钝头体模型（图 1）；2. 通过数值计算方法对比逆向射流与层板发汗组合热防护在不同攻角飞行时的流场结构和激波特性（图 6~8）；3. 通过数值计算方法获得逆向射流与层板发汗的组合热防护特性（图 9~12）。

结　论： 1. 在攻角飞行时，来流与射流方向发生偏离，且迎风面的再压缩激波增强；2. 随着攻角的增加，迎风面受热加剧，且当攻角增加到一定程度时，逆向射流热防护失效；3. 采用组合热防护系统时，发汗流的引入可以改善再附区近壁面区域的热环境，从而减少壁面的热流。

关键词： 热防护；逆向射流；层板发汗；攻角